APPLICATION

High-accuracy DLP 3D printing of closed microfluidic channels based on a mask option strategy

Zhengdong Yu[1,2] · Xiangqin Li[3,4] · Tongxing Zuo[1,2] · Qianglong Wang[1,2] · Huan Wang[1] · Zhenyu Liu[1]

Abstract

Microfluidics is a crucial technology in biological and medical fields, and its traditional fabrication methods include soft photolithography poly(dimethyl siloxane) (PDMS) technology and polymethyl methacrylate (PMMA) injection moulding technology. However, these techniques face challenges in manual alignment and bonding issues when they are used to manufacture microfluidic chips with complex flow channels. To overcome these limitations, digital light processor (DLP) 3D printing technology has been proposed as a promising alternative. However, this method is prone to problems such as channel blockage or shape distortion caused by the optical proximity effect or curing light transmission during the manufacture of microfluidic chips with small-diameter channels. This paper introduces a method to enhance the manufacturing technology by controlling the local greyscale of the projection image during DLP 3D printing. This allows for modulation of the curing light intensity, thus reducing the optical proximity effect and the impact of transmitted light on extra areas. The methodology can be employed in the production of microfluidic devices with circular and square apertures in the microchannels, utilizing commercially accessible general-purpose resins that are readily available in the market. The printed microfluidic devices show improved quality, with a channel size that closely matches the preset size, in contrast to significant channel blockage in devices printed without greyscale optimization. This method provides a new approach for enhancing the quality of low-cost microfluidic chip production and improves the print quality based on the resolution of the printer and resin used.

Keywords DLP 3D printing · Microfluidic chip · Greyscale optimization · Optical proximity effect

1 Introduction

Microfluidics is a scientific and technological discipline that focuses on the manipulation and control of small fluid volumes (typically in the range of 10^{-9} to 10^{-8} litres) in microscale systems utilizing microchannels [1–3]. Microfluidic chips have garnered significant attention in various fields, including biomedical diagnostics, food safety control, environmental protection, and animal epidemic prevention, due to their compact size, automated operation, faster detection times, reduced reagent consumption, increased sensitivity, and ability for in-field use. These chips have proven to be valuable tools for analysing biological and chemical targets and have been widely applied in these areas [4, 5]. Typically, microfluidic chips are fabricated using soft photolithography techniques with poly(dimethyl siloxane) (PDMS) [6] and polymethyl methacrylate (PMMA) injection moulding [7]. However, the fabrication processes using soft photolithography and injection moulding can be cumbersome and face challenges such as difficulties in achieving proper alignment and bonding in multilayer structures, thus hindering the precise control of fluid flow in complex 3D fluidic networks [8]. In recent years, the adoption of DLP 3D printing in the fabrication of microfluidic chips has grown significantly due to its ability to deliver high printing accuracy and ensure material continuity in printed devices. This technology has become a widely used method for producing microfluidic chips due to its advantages over traditional fabrication methods [9–12].

✉ Zhenyu Liu
liuzy@ciomp.ac.cn

[1] Changchun Institute of Optics Fine Mechanics and Physics (CIOMP), Chinese Academy of Sciences, Changchun 130033, China

[2] University of Chinese Academy of Sciences, Beijing 100049, China

[3] Beijing University of Technology, 100022 Beijing, China

[4] Shaoguan University, Shaoguan 512005, China

The primary constraint in utilizing DLP 3D printers to achieve minimum channel height printing is the propensity for overcuring the resin in the vertical direction [13, 14]. This phenomenon occurs due to the light transmitting properties of the resin, which allows for additional light to penetrate previously printed layers during the curing process. This results in the resin inside the channel becoming photopolymerized, potentially leading to partial or complete blockage of the channel. To mitigate this issue, some researchers have employed the use of an auxiliary platform during the curing process, which helps to reduce the amount of light transmitted through the resin and minimize the total energy irradiated on it, thereby preventing overcuring of the resin in the vertical direction [8]. However, the auxiliary platform method does not effectively address the optical proximity effect (OPE), which can occur when the performance of the light source is inadequate [15]. The OPE is a phenomenon influenced by the curing light, primarily resulting from the diffraction and leakage of the curing light [16]. This leads to an overcuring of the resin due to the higher intensity of the diffracted and leaked light compared to the minimum curing light required by the resin (see Fig. 1a). This issue is particularly pronounced in complex high-density microfluidic channels at right-angle cross positions in the plane perpendicular to the Z-axis direction. To mitigate the effects of the OPE, some researchers have explored fine-tuning various printing parameters, such as the distance between the construction platform and the bottom of the resin barrel, the orientation of the microfluidic channel on the build platform, and the use of specific voxel compensation methods for DLP printing devices [17]. Additionally, some researchers have proposed a mathematical approach to model the light dose profile, which can help reduce feature height errors and further optimize the printing process [18]. However, current research on the OPE and its impact on print quality in planes perpendicular to the printing direction is limited. Other researchers have attempted to mitigate the effects of the OPE by adjusting the composition of the resin to reduce the penetration depth of the curing light, thus limiting its impact on the microstructure of transparent resins during curing [19–23]. The utilization of these techniques may result in the discolouration of the printed component,

thereby hindering the subsequent assessment and examination of the fluid within the microfluidic channel [24, 25]. In contrast to the aforementioned studies that necessitate modifications to the machinery or resin, the greyscale compensation approach proposed in this paper only necessitates software-based optimization of the existing slice images. Moreover, previous studies on greyscale enhancement have primarily centred around the relationship between materials and greyscale [26], which greatly aids the implementation of the materials presented in this paper.

It is evident that the attainable scale of hole features in printer fabrication is not solely dependent on the resolution of the digital micromirror devices (DMDs) integrated in the printer but is also influenced by the optical absorption of the resin used [19]. The flushing of resin in a channel is influenced by its viscosity, as it is semicured and has a high viscosity, making the flushing process more challenging. In microfluidic channels with complex, high-density designs, a partial semicure is caused by the OPE and curing light transmission in noncured areas. When attempting to flush semicured resin using gas, the process may not be successful if the gas pressure is insufficient, and excessive pressure may cause damage to nonchannel parts. Regulating the degree of cure can, however, make flushing the resin in noncured areas more manageable and enhance the quality of subsequent processes.

In this study, we concentrate on a digital greyscale optimization technique. The method entails modifying the light intensity division by adjusting the grey value in specific regions, resulting in a closer match between the actual contour of the print and the predetermined contour (see Fig. 1b). It is worth noting that this slicing technique is similar to the open-source anti-aliasing slicing technique in that they both handle the greyscale of pixelated slicing and apply it to machining. The anti-aliasing slice approach uses grey processing to optimize the serrated edges of the created devices [27], whereas the method presented in this study uses grey processing to improve the dimensional accuracy of the manufactured devices. When used correctly, anti-aliasing softens the print's edges and reduces the staircase effect, leading to a smoother, more continuous surface [28, 29]. Furthermore, if the optimal slicing approach described in this study is

Fig. 1 Schematic representation of the OPE influence. **a** Schematic representation of the original contour relationship. **b** Schematic representation of the contour relationship after the partial region greyscale adjustment
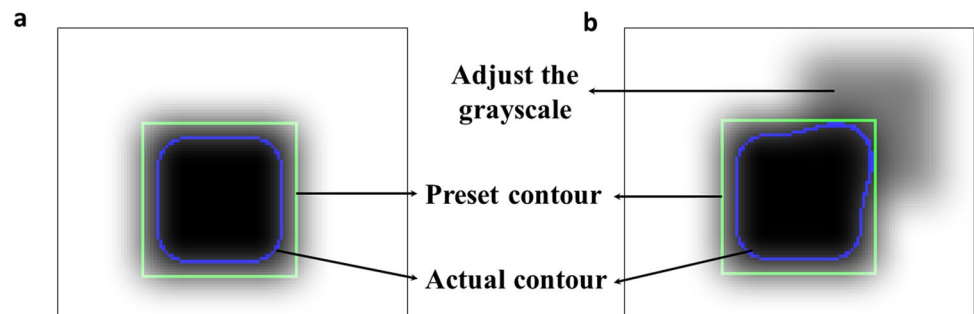
utilized properly, the microchannel, which easily becomes obstructed during the production process, can achieve the needed dimensional accuracy but also optimize the serrated edges of devices with computer control, which is more akin to the graphic compensation of the projection mask used in high-precision lithography [30].

This paper presents two main contributions. First, a collection of contour recognition methods is offered that quickly and accurately extracts contours from conventional projection images. Second, based on the extracted contours, a set of greyscale correction techniques are proposed to correct the intensity of curing light by adjusting the greyscale parameters, resolving the issues of the OPE and curing light transmission in the production of transparent devices. Specifically, we have created software to extract the contours of sliced images in 2D using the fire-burning method (FBM) [31–33] described in Section 2.4.1. Additionally, we employed homology theory [34], incorporating the tunnel loop and handle loop [35, 36], to distinguish channel-related elements from unrelated elements in 3D sliced images, as discussed in Section 2.4.2. The greyscale values of the identified contours are then adjusted based on the experimental design. These programs are integrated into a self-developed DLP 3D printer to enhance the microchannel manufacturing process. The results of the experiment show that the digital greyscale optimization method significantly improves the accuracy of microfluidic chip manufacturing.

2 Experiments

2.1 3D printer

Our laboratory has developed a 3D printer specifically for the manufacture of microfluidic devices. The two key design features of the printer are its high-resolution DMD and UV LED light source. The light intensity can be adjusted through variations in the greyscale value, a critical factor in producing different light intensities on the same print plane. The printer employs a bottom-up printing approach (see Fig. 2a), where the mechanical Z-axis controls the slice thickness to 20 μm. During printing, curing light passes through the fluorinated ethylene propylene (FEP) film to cure the resin in the vat. The cured resin on the printing platform is then removed from the FEP film by moving the platform to the next layer for subsequent curing.

The printer's optical system is based on a DLP 4710 EVM-LC from Texas Instruments, featuring a 1920 × 1080 micromirror array with a 1:1 imaging system, an imaging resolution of 20 μm and a projection area of 38.40 × 21.6 mm^2. The light engine of the light source is a 385 nm LED. We performed an experiment to determine the correlation between the greyscale values of projection images and the optical power at the curing position utilizing an optical power meter. The results are presented in Fig. 2b. The intensity of the light source was varied between 3000 and 4000 mA, which is typical for this application. Our results showed a linear relationship between the greyscale values of projection images and the optical power at the curing position. A change of 500 mA in the light current intensity was found to correspond to a change of 25–30 in the greyscale value. In summary, our self-developed 3D printer allows for the reliable control of exposure intensity in the same plane by adjusting the greyscale value of the sliced images. The relationship between the greyscale values of the projection images and the optical power at the curing position has been determined to be linear, with a change of 500 mA in light current intensity being equivalent to a greyscale value change of 25–30. This capability provides a solid foundation for further research on greyscale optimization in the manufacturing of transparent microfluidic devices.
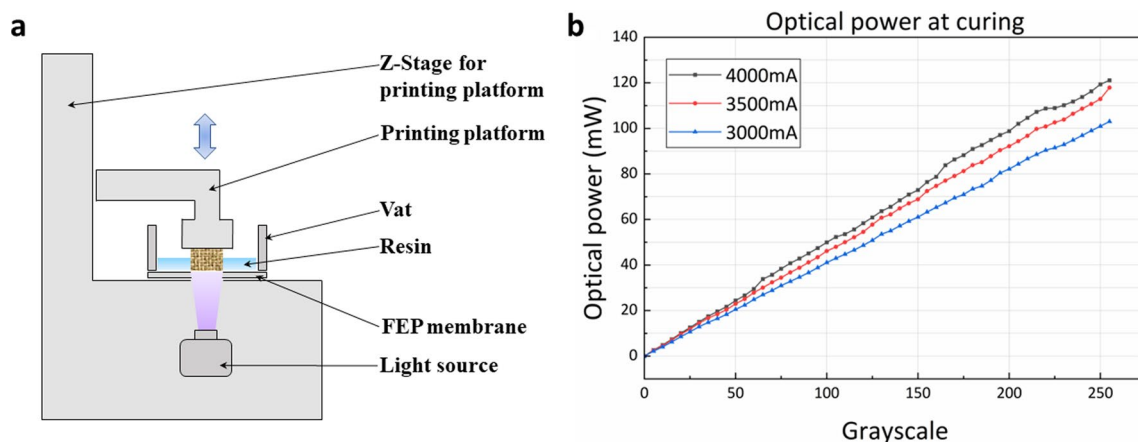

Fig. 2 **a** Design image of our DLP 3D printer. **b** The relationship between the curing light intensity and greyscale value

2.2 Materials

In this study, we chose polyethylene glycol diacrylate (PEGDA) (average Mn: 250 and 700) and ethylene glycol phenyl ether acrylate (EGPEA) as monomers, benzene bis(2,4,6-trimethylbenzoyl) phosphine oxide (commercially known as Irgacure 819) as a photoinitiator, and 2-nitrobenzylphenyl sulfide (NPS) as an ultraviolet absorber. NPS was selected to allow adjustable ultraviolet absorption [19, 37, 38]. The high transmittance and near colourless characteristics of the resin used in the 3D printer make it ideal for observing microfluidic channels and studying the influence of greyscale variations, as it is sensitive to changes in light intensity. This allows for a better understanding of the relationship between greyscale values and optical power at the curing position, which is essential for the greyscale optimization of transparent microfluidic device manufacturing. To provide a reliable basis for greyscale optimization research, we also selected a resin that was simply modified from a commercial resin for the validation of the printing method. The resin is blended with commercial resin, colouring dye, and 1,6-hexanediol diacrylate. The commercial resin, named General-rigidity Resin, was purchased from eSUN (viscosity 100–150, applicable wavelength 365–405 nm, curing shrinkage 1.86–2.12, density 1.05–1.13, tensile strength 36-52, notched impact strength 11–20, bending strength 59–70, bending modulus 1882–2385, surface hardness 88 D). The colouring dye Slover Yellow 33 was purchased from MACKLIN. The 1,6-hexanediol diacrylate, named AgiSyn 2816 HDDA, was purchased from CHREASE CHEMICAL.

2.3 Flow channel flushing

Immediately after 3D printing, it is essential to remove the residual uncured resin from the flow channels of the fabricated device. To achieve this, an isopropyl alcohol (IPA) rinse is initially employed. In cases where the residual uncured resin is not effectively removed through IPA rinsing, ultrasonic cleaning can be utilized to further aid in cleaning. Once the channels were adequately cleaned, they were dried using nitrogen to prevent any recontamination. To ensure that the residual IPA is not inadvertently reintroduced into the channels, caution is exercised during the cleaning process by directing the IPA flow through one side of the channels while utilizing a cloth to absorb any IPA that may escape through the other side of the channel outlets, thus preventing any IPA from flowing back into the channels after cleaning has ceased.

2.4 Slice optimizations

A projection image with a slice thickness of 20 μm is generated from the 3D model of the device to be printed. The image has a resolution of 1920×1080, and each pixel has a feature size of 20×20 μm. The greyscale values of the light source are set from 0 to 255, with 0 representing no light and 255 representing the highest intensity light of the printer. In the projection image, white pixels correspond to the exposed area with a greyscale value of 255, while black pixels correspond to the nonexposed area with a greyscale value of 0. Grey pixels represent the greyscale-optimized area with a set greyscale values. Based on the projection image obtained by slice (see Fig. 3a, b), to facilitate exposure intensity adjustment, we use a Python program to extract the 2D contours in projection images (see Fig. 3d, h) and use a 3D contour selection program to distinguish the channel-related and unrelated parts of the 2D contour-sliced images (see Fig. 3d, i, green arrow). Thus, the greyscale value of channel-related elements can be adjusted according to the precisely identified boundary elements (see Fig. 3d, e). Finally, Fig. 3j–l shows a schematic of the chosen greyscale optimization parameters L_{XY} and L_Z.

2.4.1 2D contour extraction

The 2D contour extraction method applied to the projection images lacks the essential 3D contour information for greyscale optimization. To address this issue, we adopt the fire-burning method (FBM) and incorporate matrix computations to calculate the connected domains. This enables us to identify the 2D contours from the greyscale images, which are derived from the projection-sliced images. The matrix computation strategy and algorithms are illustrated in Fig. 4a. Figure 4a-1 defines the four-connected domains, where if the edges of two pixels touch, they belong to the same connected domain. If the pixels belong to the same connected domain and are connected horizontally or vertically, they are considered part of the same object. Fig. 4a-3 defines the eight-connected domains, where if the edges or vertices of two pixels touch, they belong to the same connected domain. If the pixels belong to the same connected domain and are connected in horizontal, vertical, or diagonal directions, they are considered part of the same object. The values of H5 and H9 are calculated based on the defined matrix computation and the 3×3 matrix (refer to Fig. 4a-2 and 4), which are utilized to distinguish the four-connected and eight-connected domains.

The process of identifying the contours involves the following steps. First, the projection image is binarized by setting the exposed area to 1 and the nonexposed area to 0. The pixel with a value of 1 in matrix (e5) is then subjected to boundary identification using the matrix. As demonstrated in Fig. 4a-4, the eight-connected domain is identified. If the calculation of H9=8 is obtained through the arithmetic formula (as depicted in Fig. 4a-4), element (e5) is recognized as an inner element. On the other hand,
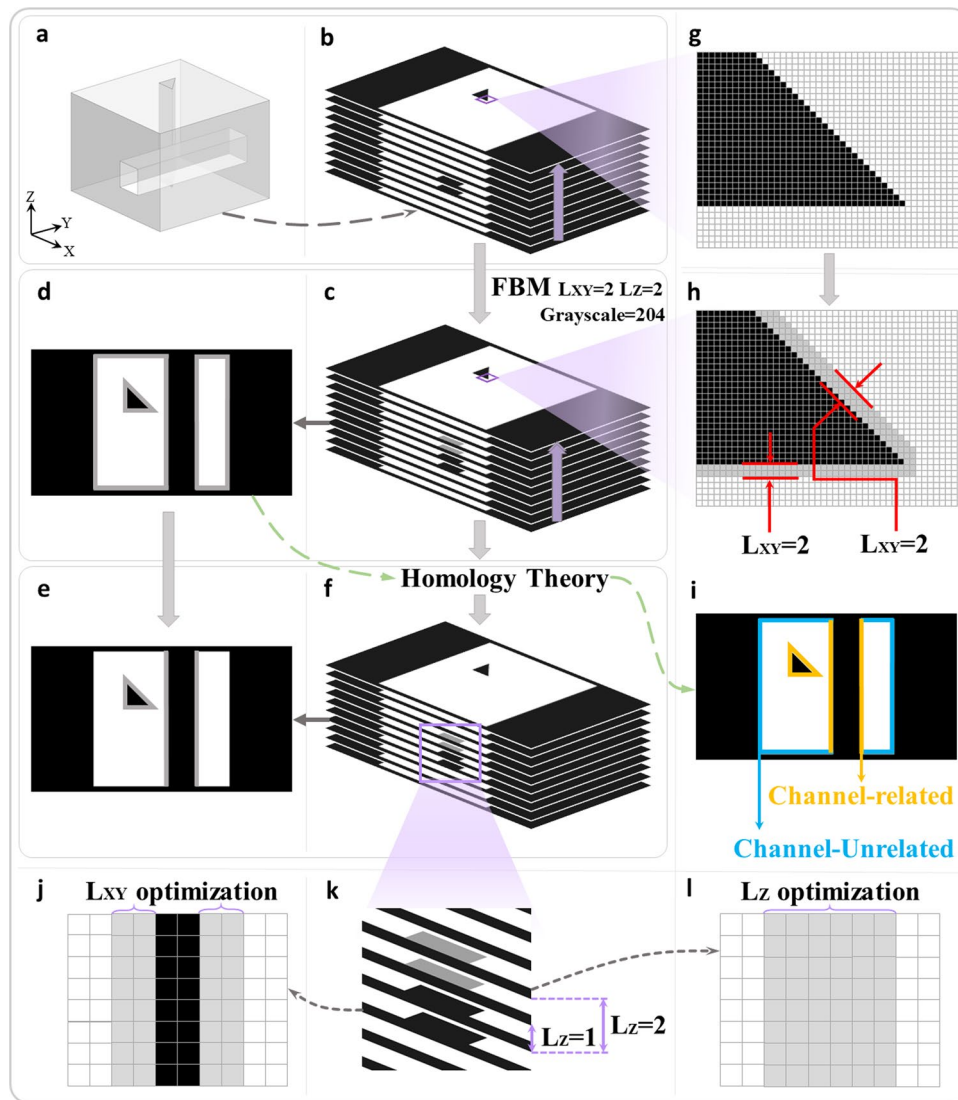
Fig. 3 A flow chart of contour recognition and greyscale optimization. **a** Selected model. **b** Schematic representation of the sliced model. **c** Schematic representation of the optimized slice of projection images by the FBM method with $L_{XY} = 2$, $L_Z = 2$, and greyscale = 204. **d** Schematic representation of projection images optimized by the FBM method. **e** Schematic representation of the projection image processed by the homology theory function. **f** Schematic representation of the slice processed by the homology theory method. **g** Schematic representation of the initial state of the projection image obtained by the initial slice. **h** Schematic representation of the projec-tion image after greyscale optimization by selecting $L_{XY} = 2$. **i** Schematic representation of channel-related and channel-unrelated structures distinguished by Fig. 3d through the homology theory method. The channel-related line is a kind of boundary line created by slicing the contour boundary of the channel in the 3D model in Fig. 3a. Channel-unrelated is a kind of boundary line that is not channel-related in all boundary lines. **j** Schematic of the L_{XY}. **k** Schematic of the L_Z. **l** The corresponding Fig. 3k is a schematic of the optimization method for the optimization layer by the L_Z selected

if H9 < 8 is obtained, element (e5) is considered a boundary element. The boundary elements are linked to form a closed ring, which constitutes a 2D contour. Finally, secondary identification is carried out on the identified boundary elements to eliminate redundant vertices from the projected image. If the secondary identification shows H5 = 0 and H9 < 2, the element is deemed a redundant element, and its value is reset to 0 in the binarized matrix.

According to the 2D contour extraction method, we can identify the connected domain of the image with a resolution of 1920 × 1080, as shown in Fig. 4b. The identification of the connected domain of the two points is shown in Fig. 4c. The element H9=8 is identified as an inner element. The element H9=4 is identified as a boundary element. If all identified contour elements are removed, the elements that are adjacent to the original contour elements will become

Fig. 4 Example of greyscale contour recognition and optimization process. **a** Adjacency of the square grid: 1 vertical or horizontal elements are considered to be four-connected, 2 identification method of four-connected, 3 vertical, horizontal, and diagonal neighbouring elements with adjacencies are considered to be eight-connected, 4 identification method of eight-connected. **b** Projection image to be optimized. **c** Feature values obtained after identification using the FBM method. **d** Optimize the greyscale of the edges and select the result of weakening the greyscale layer ($L_{XY} = 1$). **e** Optimize the internal greyscale and select the result of weakening the greyscale two layers ($L_{XY} = 2$)
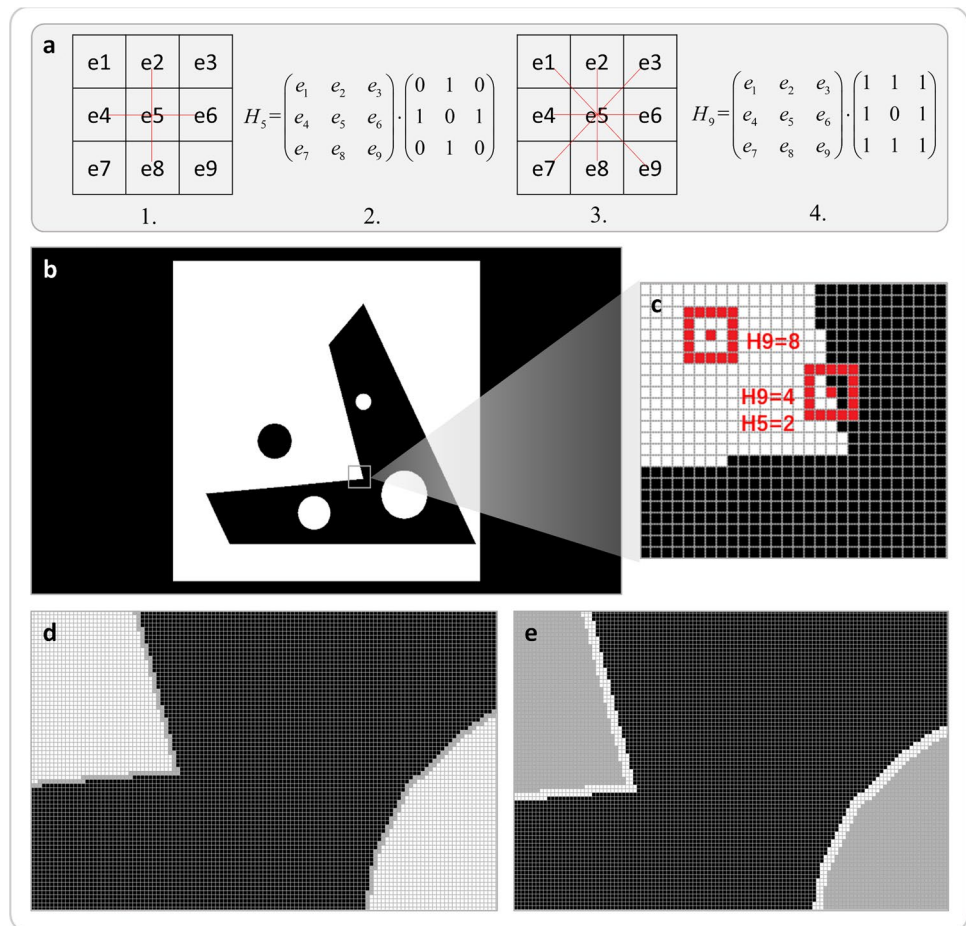
new boundary elements. The new boundary elements form a new boundary contour, which is set as the second layer of the original contour. We can extract the boundary elements with different pixel widths (pixel edge lengths or diagonal widths) by this method, as in Fig. 4d, e and in Fig. 3h, j. Finally, the greyscale values of the boundary elements can be changed according to the greyscale correction method in Section 2.5 later. Thus, the optimization of the greyscale of printing in the 2D plane is completed.

2.4.2 3D contour extraction

The 2D contour extraction method cannot identify the top of the channel in a single-slice direction when the position of the acquired projection image in the Z-axis direction of the sliced layer is higher than or equal to the top of the microfluidic channel. In addition, the elements of the blue line (see Fig. 3i channel-unrelated) and the yellow line (see Fig. 3i channel-related) have the same meaning in this method. Thus, the 2D contour extraction method used in the recognition of the projection image shown in Fig. 3i cannot identify whether the contour elements are channel-related from the projection image containing the through-hole.

Due to the grey-optimized edges, the curing light intensity is insufficient, which will lead to a soft structure in the channel-unrelated part. If the manufacturing quality and hardness of the channel-unrelated part of the microfluidic chip is not high, then it is possible to use only the 2D contour extraction method for greyscale optimization. The top information of the channel could be selected by 2D contour selection on another sliced plane, whose direction is requested to be perpendicular to the original slicing direction. Thus, all the 3D contour extraction is completed. However, if devices with high manufacturing quality are needed, a distinction between channel-related and channel-unrelated in greyscale optimized contour extraction is needed. This prevents impairing the exposure intensity of channel-unrelated areas that do not need to be weakened. Therefore, we further investigate the method of 3D contour extraction to identify and distinguish the areas that are channel-related and channel-unrelated.

It is worth noting that the 3D contour identification in this paper refers to the identification of the flow channel surface, but the 3D contour identification is relatively complex, and the core goal of this paper is to verify the feasibility of the greyscale optimization method. Thus, this paper only

identifies the three-dimensional contour of the microfluidic device, in which each flow channel cross section remains constant; therefore, the three-dimensional contour identification problem is simplified to the flow channel cross-section identification problem. The first step is to reconstruct the 3D model based on the slices: read the sliced images of the printed model and convert the images into a greyscale matrix, where the solid part is 1 and the nonsolid part is 0. Then, the greyscale matrix is arranged sequentially at 20 μm intervals, thus forming a 3-dimensional numerical matrix. The surface mesh of the microfluidic device is reconstructed according to the 3D numerical matrix, and the algorithm of Dey et al. [35] is used to calculate the tunnel loops and handle loops, thus completing the identification of the flow channel cross-section of the desired printed model based on the sliced images, thereby providing support for more accurate channel-related parameter identification for greyscale optimization.

The flow channel cross section is closely related to the geometric feature called the tunnel loop in the 3D model. There exists a special set of nontrivial loops on the surface called tunnel and handle loops that are closely related to the geometric features called tunnel and handle loops in the 3D model, respectively, where this special set of nontrivial loops is also known as the 1-dimensional homology group in homology theory. Therefore, this paper identifies the 3D contours (tunnel loops) by homology theory. Let M be a connected, closed (compact and without boundary), and orientable surface. Such a surface M partitions R^3 into two regions I and O such that I∩O = M and I∪O = R^3. The unbounded region O is called the exterior of M, while the bounded region I is the interior of M. For a disjoint simple closed curve γ on M, if γ is trivial in O but nontrivial in I, then it is a tunnel loop; similarly, if γ is trivial in I but nontrivial in O, then it is a handle loop. In other words, if γ can be continuously reduced to a point in O but not in I, then it is a tunnel loop; similarly, if γ can be continuously reduced to a point in I but not in O, then it is a handle loop. It is worth noting that the tunnel loop and the handle loop are symbiotic, i.e., if there is a tunnel loop, there must be a corresponding handle loop, and vice versa. Furthermore, the number of tunnel loops (or the number of handle loops) on M is equal to its genus. The genus represents the maximum number of

cuttings along nonintersecting closed simple curves without rendering the resultant structure disconnected. In addition, there are infinitely many sets of tunnel loops on the surface, and the tunnel loops in the article default to a set of shortest length tunnel loops. The genera of the surfaces shown in Fig. 5a–c are 1, 2, and 3, respectively; thus, they have 1, 2, and 3 shortest tunnel loops (red loops), respectively.

The information of the channel-related boundary is extracted based on this method (as shown in Fig. 5d). Then, the channel-unrelated part of the 2D contour recognition image is removed using this information. Then, coordinate information of the elements in the channel-related part and the channel top part is extracted. It can be adjusted to optionally modify only the greyscale value of a single parameter (L_{XY} and L_Z described in Section 2.5, choose one of them for modification), which is convenient for variable control.

2.5 Greyscale adjustment

The greyscale values of the boundary elements determined by the projection images extracted based on the method in Section 2.4 are adjusted. The number of contour layers in the projection image (Fig. 3h, j) is set to L_{XY}. The number of layers in the optimized slice (Fig. 3k) is set to L_Z. The L_Z-optimized part is modified according to the L_{XY}-optimized part in the way shown in Fig. 3j–l. By a single variable adjustment, the L_{XY} mainly influences the OPE, and the L_Z mainly influences the cured light transmission. Square aperture channels with feature size D_L in the vertical or parallel to the print plane direction are performed to check the effect of the set parameters on the quality of the channels. If a single parameter could not complete the optimization, reducing the greyscale value of the greyscale optimization part could further reduce the light intensity of the exposure region. Meanwhile, increasing L_Z and L_{XY} could increase the impact range. These strategies enhance the optimization effect.

2.5.1 L_{XY} adjustment

To improve the print quality of the holes in the vertical direction, as shown in Fig. 6a, we used the greyscale optimization method to print square microfluidic channels with
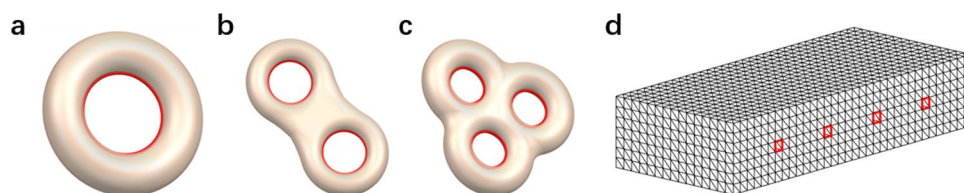

Fig. 5 Identification of the shortest tunnel loops. **a** Genus is 1. **b** Genus is 2. **c** Genus is 3. **d** Identify the outline circle of the solid microfluidic channel to be printed; the red circle is the extracted boundary of the channel-related channel
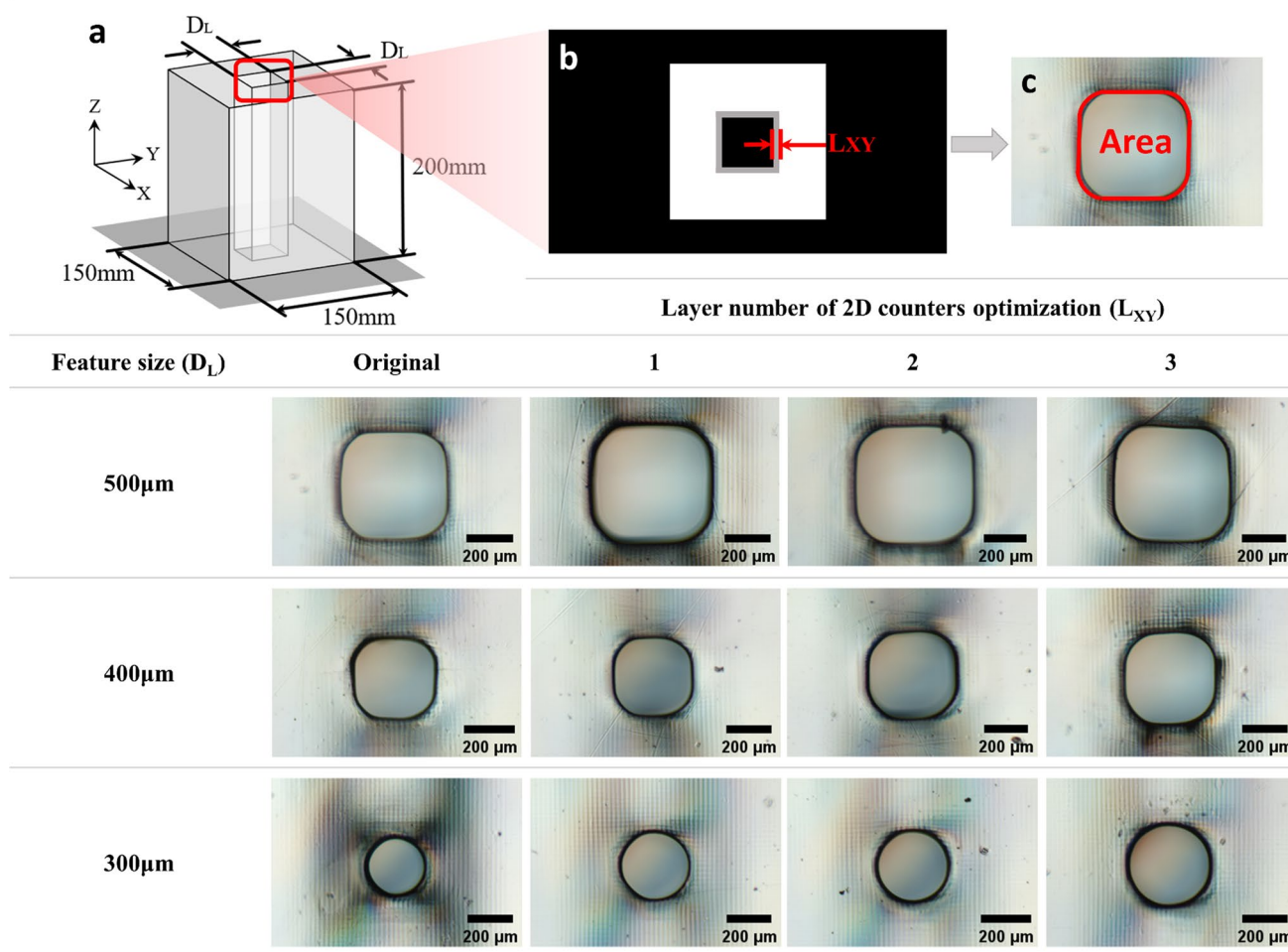
Fig. 6 The print experiment was conducted for the 300–500 μm flow channel for different layers (L_{XY}) of pixels after greyscale optimization, and the print size was closest to the preset size after three layers of greyscale optimization with a stripe width of 20 μm on the result. **a** Schematic representation of the size of the printed model. **b** Schematic representation of the optimization of the printed model. **c** Schematic representation of the printing results and an illustration of the evaluation criteria area

different feature sizes D_L by only changing the parameter L_{XY}. According to the contour selection method introduced in Section 2.4, we adjusted the optimization range of the 2D greyscale by $L_{XY} = 1\sim3$. The greyscale value was chosen to be 10% higher than the cure threshold of the resin. Therefore, the overcured resin in the greyscale optimized area could be cleaned more easily. Thus, the OPE on the overcuring area of the resin is reduced.

The experimental results are measured according to the stripe width or square grid edge length (20 μm, approximate pixel resolution width) left on the model surface during printing, as shown in Fig. 6. The greyscale improvement method could significantly improve the quality of the microchannel. The area of the effective cross-section of the channel shown in Fig. 6c is used as the evaluation criterion. The results of this experiment show that the area of the cross-section of the channels after greyscale optimization

using $L_{XY} = 3$ is approximately 95% of the preset area. In contrast, the area of the cross section of the channels without optimization is approximately 80% of the area of the preset. In addition, if more greyscale-optimized layers are applied, there is less residual resin in the channels after cleaning. It is confirmed that proper adjustment of the L_{XY} has an improved effect on print quality.

2.5.2 L_Z adjustment

To improve the print quality of the holes in the parallel direction (shown in Fig. 7a), we used the greyscale optimization method to print square microchannels by only adjusting L_Z. As Fig. 7a shows, the feature size of the printed model is $D_L = 400$ μm~500 μm, which parallels the plane of printing. To reduce OPE from the effect of curing light transmission, we chose a large width of the channel. This could facilitate the
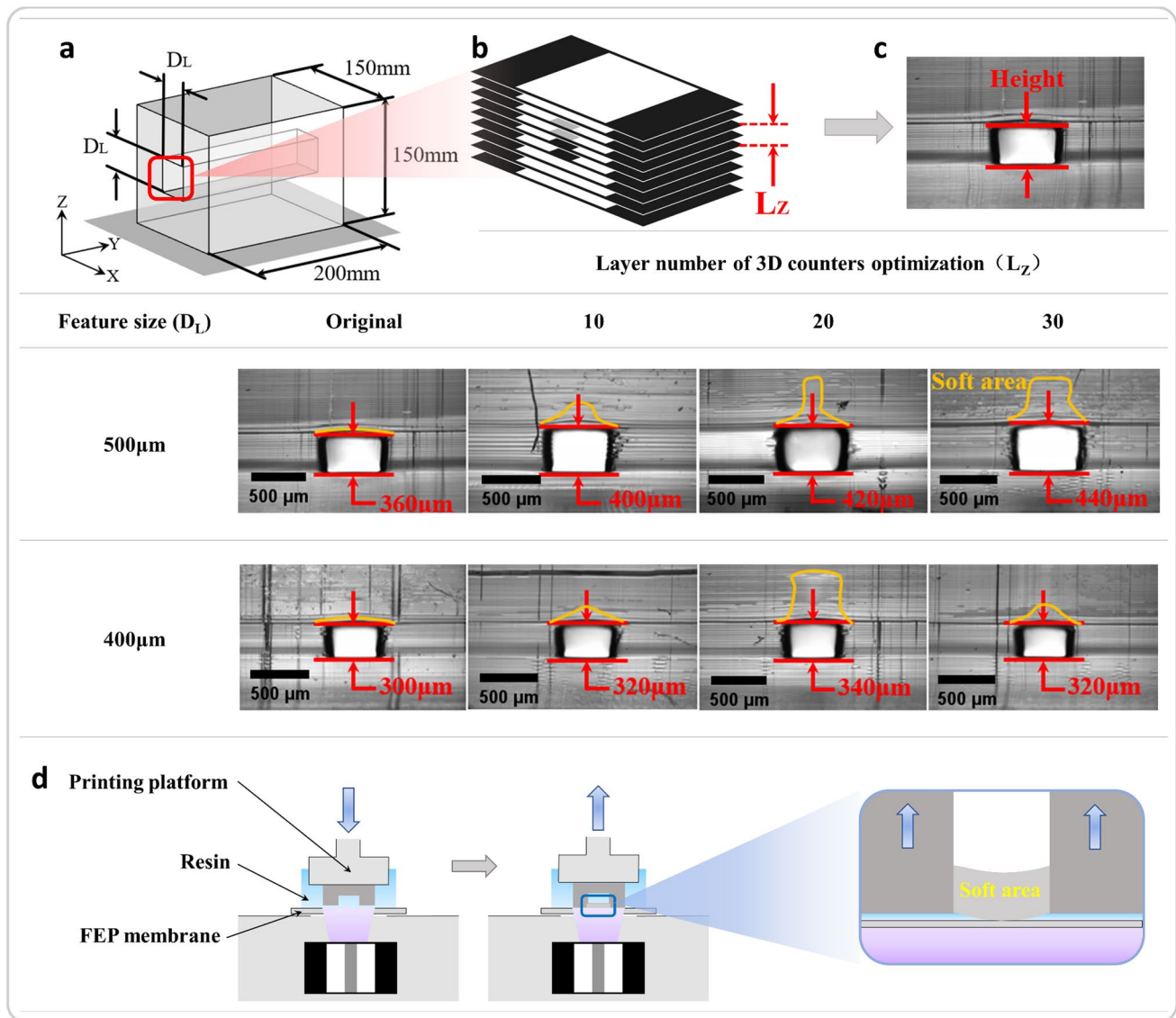
Fig. 7 Printing experiments after greyscale optimization of different layers (L_Z) of pixels for the 500 μm flow channel. **a** Schematic representation of the print model size. **b** Schematic representation of the print model slice optimization. **c** Schematic representation of the printing effect and evaluation criteria height. **d** Schematic representation of the process of soft area production

observation of the size of the cured resin and the state of the semicured resin affected by curing light transmission. We adjusted L_Z from 10 to 30 for greyscale optimization. The greyscale value is approximately equal to the cure threshold of the resin.

In this experiment, the thickness of each printed layer is approximately 20 μm. Compared to the devices without greyscale optimization, it can be observed that the optimized part has a softer structure (see Fig. 7) due to the adjustment intensity of the curing light. The soft structure was distorted when separated from the FEP film, which caused a small malformation of the printed devices (see Fig. 7d). The effective height of the channel shown in

Fig. 6c is used as the evaluation criterion. For the preset height $D_L = 500$ μm, the height of the printed channel after greyscale optimization is approximately 88% of the preset height with the parameter $L_Z = 30$, which is 16% higher than the 72% obtained by the device manufactured without optimization. For the preset $D_L = 400$-μm device, the results after optimizing height do not change significantly. It is worth noting that this does not mean that the optimization of L_Z is invalid. This phenomenon probably occurred due to the small size of the chosen channel, which suffered a larger effect of OPE than a large width due to the instability of the machine. We can overcome this issue by adjusting L_{XY}. That is, the instability of the

machine can be overcome to some extent by adjusting L_{XY} and L_Z.

3 Experiment and discussion

It is worth noting that the resin we used in this experiment is remade by a common commercial resin. Because the circular microfluidic channel can simultaneously examine the effect of L_{XY} and L_Z, we printed a set of orthogonal droplet generators with circular holes in the microchannels with a 500 μm diameter, as shown in Fig. 8a. In this experiment, we take $L_Z = 50$ for greyscale optimization with greyscale as the primary variable. After the print quality stabilized, the print experiment only used L_{XY} as the variable. The experimental results are shown in Fig. 8. There is a residue of uncured or semicured resin in these cases without greyscale optimization or when the parameters of greyscale optimization are not selected exactly. In addition, as the greyscale values decrease and L_{XY} increases, the print channel size gradually approaches the preset size. As shown in Fig. 8e, f, the device pictures of the corresponding photomicrographs taken before and after greyscale optimization are shown. The experimental results demonstrate the feasibility of the greyscale optimization method to improve the print quality of highly transparent devices.

We found that reducing the greyscale values of the optimization also significantly attenuated the overcuring problem. In addition, as the experimental results show, the optimized position can still be cured even when the greyscale values of the optimized part are lower than the cure threshold of the resin. We speculate that this phenomenon is caused by the excessive amount of cure initiator used in this resin, which is easily influenced by the cure light from OPE. Therefore, we increased the values of L_{XY}. The experimental results approximated the anticipated results. Following this line of experimentation, the suitable values of greyscale optimization parameters that produce better print results can be approximated by a few simple sets of experiments using common resins.

Fig. 8 Printed orthogonal droplet generators with circular flow channels of 500 μm radius. **a** Schematic representation of the dimensions of the circular orifice runner of the printed device. **b** 3D model drawing of the printed device. **c** The parameters selected for the greyscale optimization of the device correspond to the imaginary exposure schematic of the cross section of the device, as shown in (b). **d** Schematic representation of the greyscale optimization of the channel. **e** Photomicrographs of devices manufactured before greyscale optimization and physical drawings. **f** The physical picture and micrographs of the fabricated device after adjustment for greyscale optimization using the parameters greyscale = 128, L_{XY} = 6, and L_Z = 50
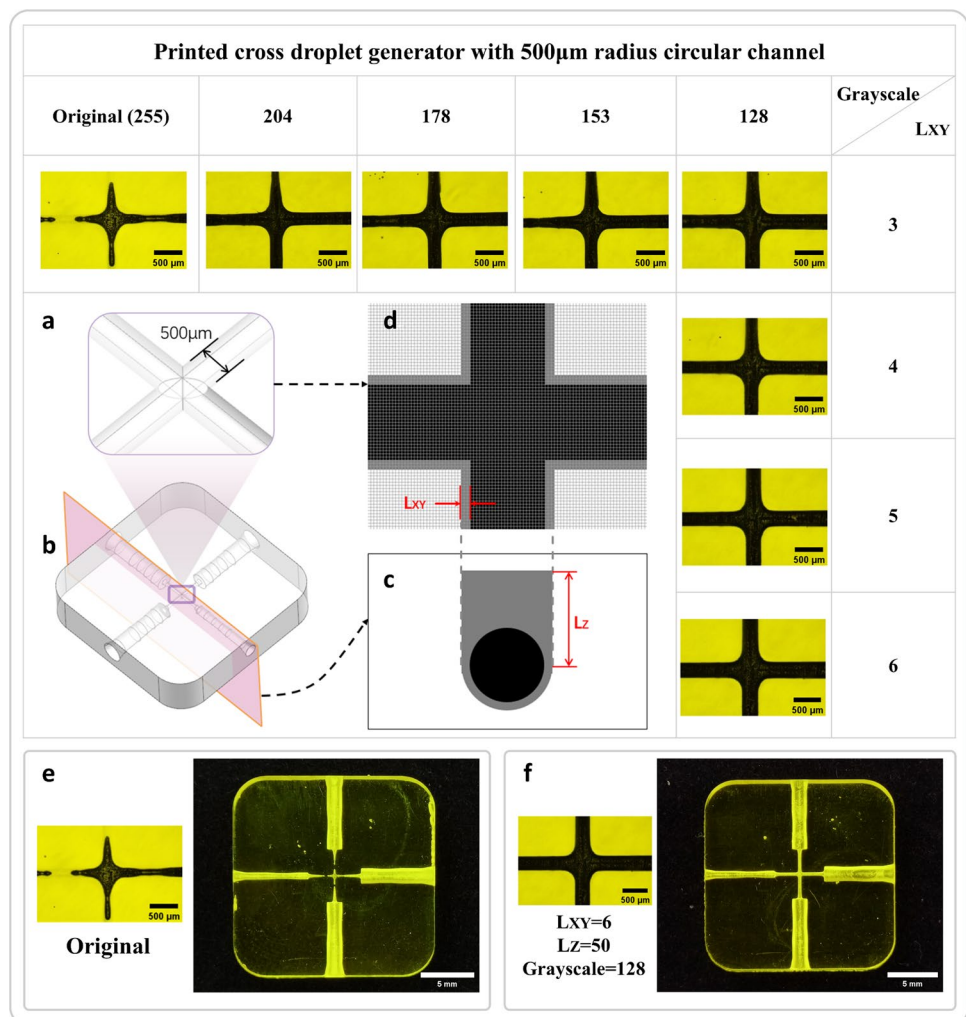
4 Conclusions

In summary, a greyscale optimization method is presented to print microsized channels using light-curing resins with high light transmittance. The method can improve the accuracy of the positioning of resin curing performance, which includes a set of methods of extracting model contour information in sliced images and offers a set of methods to choose parameters of the greyscale-optimized strategy. The purpose of controlling the light intensity of curing light in the hollow channel region and adjacent designated areas is achieved. By the method presented, the effect of OPE and curing light transmission due to the high light transmission of the resin on the minimum size of the printed microfluidic channel has been impaired. This method can further improve the manufacturing quality under the same conditions as the DLP 3D printer and general commercial resin. This is not limited to the printer resolution used in this article, contributing to the development of one-step preparation of microfluidic chip channels using DLP 3D printers. Overall, the method can also enhance the fabrication quality of complex and high-density microfluidic channels in printed microfluidic chips. This study provides a new strategy for quality improvement and iterative updates of low-cost microfluidic chip preparation.

In addition, we believe that the 3D contour recognition strategy described in Section 2.4.2 of the paper can be extended to recognize 3D contours of chips with complex flow channels, but the specific details deserve further investigation. We believe that the 3D skeleton technique [39] can also be used to identify accurate 3D contours of complex flow channels in microfluidic chips. Furthermore, we will also research this method's automatic global optimization.

Author contribution Zhengdong Yu: conceptualization (lead); data curation (equal); investigation (equal); software (equal); validation (equal); writing—original draft (equal); writing—review and editing (equal). Xiangqin Li: formal analysis (equal); investigation (equal); resources (equal); software (supporting); validation (equal); writing—review and editing (equal). Tongxing Zuo: data curation (equal); software (equal); writing—original draft (equal); writing—review and editing (equal). Qianglong Wang: resources (equal); validation (equal). Huan Wang: resources (supporting); writing—review and editing (equal). Zhenyu Liu: investigation (equal); formal analysis (equal); supervision (lead); resources (supporting); writing—review and editing (equal).

Declarations

Competing interests There authors declare no competing interests.

References

1. Seemann R, Brinkmann M, Pfohl T, Herminghaus S (2012) Droplet based microfluidics. Rep Prog Phys 75:016601. https://doi.org/10.1088/0034-4885/75/1/016601

2. Song Y, Michaels TCT, Ma Q, Liu Z, Yuan H, Takayama S, Knowles TPJ, Shum HC (2018) Budding-like division of all-aqueous emulsion droplets modulated by networks of protein nanofibrils. Nat Commun 9:2110. https://doi.org/10.1038/s41467-018-04510-3

3. Shang L, Yu Y, Liu Y, Chen Z, Kong T, Zhao Y (2019) Spinning and applications of bioinspired fiber systems. ACS Nano 13:2749–2772. https://doi.org/10.1021/acsnano.8b09651

4. Bein A, Shin W, Jalili-Firoozinezhad S, Park M, Sontheimer-Phelps A, Tovaglieri A, Chalkiadaki A, Kim HJ, Ingber DE (2018) Microfluidic organ-on-a-chip models of human intestine. Cell Mol Gastroenterol Hepatol 5:659–668. https://doi.org/10.1016/j.jcmgh.2017.12.010

5. Cai G, Xue L, Zhang H, Lin J (2017) A review on micromixers. Micromachines 8:274. https://doi.org/10.3390/mi8090274

6. Qin D, Xia Y, Whitesides GM (2010) Soft lithography for micro- and nanoscale patterning. Nat Protoc 5:491–502. https://doi.org/10.1038/nprot.2009.234

7. Lei KF, Law WC, Suen Y-K, Li WJ, Yam Y, Ho PH, Kong S-K (2007) A vortex pump-based optically-transparent microfluidic platform for biotech and medical applications. Proc Inst Mech Eng Part H-J Eng Med 221:129–141. https://doi.org/10.1243/09544119JEIM189

8. Xu Y, Qi F, Mao H, Li S, Zhu Y, Gong J, Wang L, Malmstadt N, Chen Y (2022) In-situ transfer vat photopolymerization for transparent microfluidic device fabrication. Nat Commun 13:918. https://doi.org/10.1038/s41467-022-28579-z

9. Beauchamp MJ, Nordin GP, Woolley AT (2017) Moving from millifluidic to truly microfluidic sub-100-μm cross-section 3D printed devices. Anal Bioanal Chem 409:4311–4319. https://doi.org/10.1007/s00216-017-0398-3

10. Mehta V, Rath SN (2021) 3D printed microfluidic devices: a review focused on four fundamental manufacturing approaches and implications on the field of healthcare. Bio-Des Manuf 4:311–343. https://doi.org/10.1007/s42242-020-00112-5

11. Wang J, Shao C, Wang Y, Sun L, Zhao Y (2020) Microfluidics for medical additive manufacturing. Engr 6:1244–1257. https://doi.org/10.1016/j.eng.2020.10.001

12. Fritschen A, Bell AK, Königstein I, Stühn L, Stark RW, Blaeser A (2022) Investigation and comparison of resin materials in transparent DLP-printing for application in cell culture and organs-on-a-chip. Biomater Sci 10:1981–1994. https://doi.org/10.1039/D1BM01794B

13. Jacobs PF (1993) Rapid prototyping & manufacturing— fundamentals of stereolithography. J Manuf Syst 12:430–433. https://doi.org/10.1016/0278-6125(93)90311-g

14. Jariwala AS, Ding F, Zhao X, Rosen DW (2010) A process planning method for thin film mask projection micro-stereolithography. In: Asme International Design Engineering Technical Conferences and Computers and Information in Engineering Conference, Proceedings, vol 2. Pts a and B. Amer Soc Mechanical Engineers, New York, pp 685–694

15. Yen A, Tzviatkov P, Wong A, Juffermans C, Jonckheere R, Jaenen P, Garofalo J, Otto O, Ronse K, den hove Van L (1996) Optical proximity correction for 0.3 μm i-line lithography. Microelectron Eng 30:141–144. https://doi.org/10.1016/0167-9317(95)00213-8

16. Huo F, Wang W, Xue C (2016) Limits of scalar diffraction theory for multilayer diffractive optical elements. Optik 127:5688–5694. https://doi.org/10.1016/j.ijleo.2016.03.062

17. Maennel M, Selzer L, Bernhardt R, Thiele J (2019) Optimizing process parameters in commercial micro-stereolithography for forming emulsions and polymer microparticles in nonplanar microfluidic devices. Adv Mater Technol 4:1800408. https://doi.org/10.1002/admt.201800408

18. Pritchard ZD, de Beer MP, Whelan RJ, Scott TF, Burns MA (2019) Modeling and correcting cure-through in continuous stereolithographic 3D printing. Adv Mater Technol 4:1900700. https://doi.org/10.1002/admt.201900700

19. Gong H, Beauchamp M, Perry S, Wolley AT, Nordin GP (2015) Optical approach to resin formulation for 3D printed microfluidics. RSC Adv 5:106621–106632. https://doi.org/10.1039/C5RA23855B

20. Rogers CI, Qaderi K, Woolley AT, Nordin GP (2015) 3D printed microfluidic devices with integrated valves. Biomicrofluidics 9:016501. https://doi.org/10.1063/1.4905840

21. Urrios A, Parra-Cabrera C, Bhattacharjee N, Gonzalez-Suarez AM, Rigat-Brugarolas LG, Nallapatti U, Samitier J, DeForest CA, Posas F, Garcia-Cordero JL, Folch A (2016) 3D-printing of transparent bio-microfluidic devices in PEG-DA. Lab Chip 16:2287–2294. https://doi.org/10.1039/C6LC00153J

22. Lee Y-S, Bhattacharjee N, Folch A (2018) 3D-printed quake-style microvalves and micropumps. Lab Chip 18:1207–1214. https://doi.org/10.1039/C8LC00001H

23. Kuo AP, Bhattacharjee N, Lee Y-S, Castro K, Kim YT, Folch A (2019) High-precision stereolithography of biomicrofluidic devices. Adv Mater Technol 4:1800395. https://doi.org/10.1002/admt.201800395

24. Gong H, Woolley AT, Nordin GP (2016) High density 3D printed microfluidic valves, pumps, and multiplexers. Lab Chip 16:2450–2458. https://doi.org/10.1039/C6LC00565A

25. Gong H, Bickham BP, Woolley AT, Nordin GP (2017) Custom 3D printer and resin for 18 µm × 20 µm microfluidic flow channels. Lab Chip 17:2899–2909. https://doi.org/10.1039/C7LC00644F

26. Valizadeh I, Al Aboud A, Dörsam E, Weeger O (2021) Tailoring of functionally graded hyperelastic materials via grayscale mask stereolithography 3D printing. Addit Manuf 47:102108. https://doi.org/10.1016/j.addma.2021.102108

27. Panerai FM, Juday RD (1996) In: Tescher AG (ed) Probabilistic anti-aliasing methods for dynamic variable resolution images. SPIE, Denver, CO, pp 130–138

28. Song H-C, Ray N, Sokolov D, Lefebvre S (2017) Anti-aliasing for fused filament deposition. Comput-Aided Des 89:25–34. https://doi.org/10.1016/j.cad.2017.04.001

29. How to Use Anti-Aliasing for Resin 3D Printing – Best Settings – 3D Printerly. https://3dprinterly.com/how-to-use-anti-aliasing-for-resin-3d-printing-best-settings/. Accessed 22 May 2023

30. Burkhardt M, Yen A, Progler C, Wells G (1998) Illuminator design for the printing of regular contact patterns. Microelectron Eng 41:91–95. https://doi.org/10.1016/S0167-9317(98)00020-3

31. Han H, Guo Y, Chen S, Liu Z (2021) Topological constraints in 2D structural topology optimization. Struct Multidiscip Optim 63:39–58. https://doi.org/10.1007/s00158-020-02771-5

32. Zuo T, Wang C, Han H, Wang Q, Liu Z (2022) Explicit 2D topological control using SIMP and MMA in structural topology optimization. Struct Multidiscip Optim 65:293. https://doi.org/10.1007/s00158-022-03405-8

33. Wang Q, Han H, Wang C, Liu Z (2022) Topological control for 2D minimum compliance topology optimization using SIMP method. Struct Multidiscip Optim 65:38. https://doi.org/10.1007/s00158-021-03124-6

34. Zuo T, Han H, Liu Z (2023) Explicit tunnels and cavities control using SIMP and MMA in structural topology optimization. Comput-Aided Des 158:103482. https://doi.org/10.1016/j.cad.2023.103482

35. Dey TK, Fan F, Wang Y (2013) An efficient computation of handle and tunnel loops via Reeb graphs. ACM Trans Graph 32:1–10. https://doi.org/10.1145/2461912.2462017

36. Dey TK, Li K, Sun J (2007) On computing handle and tunnel loops. In: Wolter FE, Sourin A (eds) 2007 International Conference on Cyberworlds, Proceedings. Ieee Computer Soc, Los Alamitos, pp 357–366

37. Borrello J, Nasser P, Iatridis JC, Costa KD (2018) 3D printing a mechanically-tunable acrylate resin on a commercial DLP-SLA printer. Addit Manuf 23:374–380. https://doi.org/10.1016/j.addma.2018.08.019

38. Ahmed I, Sullivan K, Priye A (2022) Multi-resin masked stereolithography (MSLA) 3D printing for rapid and inexpensive prototyping of microfluidic chips with integrated functional components. Biosensors 12:652. https://doi.org/10.3390/bios12080652

39. Lee TC, Kashyap RL, Chu CN (1994) Building skeleton models via 3-D medial surface axis thinning algorithms. CVGIP: Graph Models and Image Process 56:462–478. https://doi.org/10.1006/cgip.1994.1042